

Self-shielding of hydrogen in the IGM during the epoch of reionization

Jonathan Chardin^{1*}, Girish Kulkarni¹ and Martin G. Haehnelt¹

¹*Institute of Astronomy and Kavli Institute of Cosmology, University of Cambridge, Madingley Road, Cambridge CB3 0HA, UK*

Accepted —. Received —; in original form —

ABSTRACT

We investigate self-shielding of intergalactic hydrogen against ionizing radiation in radiative transfer simulations of cosmic reionization carefully calibrated with Ly α forest data. While self-shielded regions manifest as Lyman-limit systems in the post-reionization Universe, here we focus on their evolution during reionization (redshifts $z = 6$ – 10). At these redshifts, the spatial distribution of hydrogen-ionizing radiation is highly inhomogeneous, and some regions of the Universe are still neutral. After masking the neutral regions and ionizing sources in the simulation, we find that the hydrogen photoionization rate depends on the local hydrogen density in a manner very similar to that in the post-reionization Universe. The characteristic physical hydrogen density above which self-shielding becomes important at these redshifts is about $n_{\text{H}} \sim 3 \times 10^{-3} \text{ cm}^{-3}$, or ~ 20 times the mean hydrogen density, reflecting the fact that during reionization photoionization rates are typically low enough that the filaments in the cosmic web are often self-shielded. The value of the typical self-shielding density decreases by a factor of 3 between redshifts $z = 3$ and 10, and follows the evolution of the average photoionization rate in ionized regions in a simple fashion. We provide a simple parameterization of the photoionization rate as a function of density in self-shielded regions during the epoch of reionization.

Key words: radiative transfer – methods: numerical – dark ages, reionization, first stars – intergalactic medium

1 INTRODUCTION

The epoch of hydrogen reionization is thought to have begun with the formation of the first sources of radiation in high-density peaks of the collapsing large-scale structure in the Universe (Gnedin 2000; Barkana & Loeb 2001; Choudhury & Ferrara 2005). Escaping Lyman continuum photons from these sources create growing H II regions around them, which grow and merge with H II regions associated with other ionizing sources (Shapiro & Giroux 1987; Anderson et al. 2016; Mutch et al. 2016; Sharma et al. 2017). Reionization is said to be complete when these ionized regions percolate, fill the cosmic volume, and establish a metagalactic UV background (Miralda-Escudé et al. 2000). Current constraints from Ly α and CMB data suggest that hydrogen reionization was complete at redshift $z \gtrsim 6$ (Robertson et al. 2015; Mitra et al. 2015; Planck Collaboration 2016; Barnett et al. 2017).

Although the Universe is highly ionized at redshifts $z < 6$, the densest regions of the cosmic web remain neutral due to high recombination rates (Miralda-Escudé et al.

2000; Choudhury et al. 2009). These neutral islands span a range of different neutral hydrogen column densities and are said to have self-shielded against hydrogen-ionizing radiation (Rahmati et al. 2013). Self-shielding is increasingly effective as the column density N_{HI} exceeds $\sim 1/\sigma \approx 10^{17} \text{ cm}^2$, where σ is the frequency-dependent ionization cross-section of hydrogen. In the post-reionization Universe, such systems are observed as Lyman-limit systems in the spectra of distant sources such as quasars (e.g., Worseck et al. 2014). The abundance of these self-shielded systems depends on the cosmological gas density distribution and the amplitude of the relatively uniform hydrogen photoionizing background. Modern cosmological simulations successfully reproduce the observed abundance and column density distribution of these self-shielded systems at redshifts $z = 2$ – 5 in the post-reionization Universe (McQuinn et al. 2011; Altay et al. 2013).

On the other hand, properties of self-shielded regions before the completion of reionization, at redshifts $z \gtrsim 6$, are less well-understood. Self-shielded regions at these redshifts represent the residual neutral hydrogen content in H II regions. But H II regions associated with individual sources of ionizing radiation have still not overlapped at

* E-mail: jc@ast.cam.ac.uk

these redshifts. As a result, the hydrogen photoionization rate has large spatial fluctuations (Chardin et al. 2015). Under such conditions, simulating the abundance and other properties of self-shielded regions requires an accurate treatment of reionizing sources and the photoionization rate fluctuations (Furlanetto & Oh 2005; Kaurov & Gnedin 2013, 2014). These high-redshift Ly α -limit systems are important as they can affect the interpretation of observations such as the rapid decrease in the abundance of Ly α emitters (Choudhury et al. 2009; Bolton & Haehnelt 2013; Choudhury et al. 2015; Mesinger et al. 2015; Keating et al. 2015). As a reservoir of neutral gas, they can also affect the 21 cm signal from the epoch of reionization, which is being targeted by many ongoing and upcoming experiments (Sobacchi & Mesinger 2014; Watkinson et al. 2015; Shukla et al. 2016; Kulkarni et al. 2016).

In this paper, we present high-resolution radiation hydrodynamics cosmological simulations of the intergalactic medium during the epoch of reionization, and characterize the density scale at which self-shielding occurs under a range of assumptions regarding the ionizing sources. These simulations are calibrated to reionization constraints from CMB and Ly α data following the procedure adopted by Chardin et al. (2015). The simulations presented by Chardin et al. (2015) were able to reproduce the evolution of the UV luminosity function of galaxies during and after reionization while at the same time reproducing a range of IGM properties inferred from observations of the Ly α forest in the post-reionization phase. We use similar simulations in the present study to investigate the evolution of the self-shielding properties of hydrogen during and after reionization. We describe our simulations, and give details of the reionization histories considered in this paper in Section 2. We discuss self-shielding in our simulations in Section 3. In Section 4, we test our results for numerical convergence and dependence on ionizing source properties, and summarise our conclusions in Section 5. Our Λ CDM cosmological model has $\Omega_b = 0.048$, $\Omega_m = 0.3175$, $\Omega_\Lambda = 0.6825$, $h = 0.6711$, $n = 0.9624$, $\sigma_8 = 0.8344$, and $Y_{\text{He}} = 0.24$ (Planck Collaboration et al. 2014).

2 SIMULATIONS

The simulations presented in this paper are performed in two steps. Hydrodynamical cosmological simulations are run as a first step, as described in more detail by Chardin et al. (2015, 2017). As the second step, sources of hydrogen-ionizing radiation are set up in the simulation box, and radiative transfer calculations are performed.

The cosmological simulations of the evolution of the dark matter and gas hydrodynamics were performed using the RAMSES code (Teyssier 2002). The simulation evolves 512^3 dark matter particles. Gas hydrodynamics is evolved on a coarse, fixed grid discretized in 512^3 cells. We did not employ the adaptive mesh refinement option of RAMSES. Although we later post-process this cosmological simulation for radiative transfer, we also implement a uniform UV background model in the simulation to get a realistic gas density structure. We use the metagalactic UV background model of Haardt & Madau (2012, HM12 hereafter), in which the time evolution of the space-averaged UV background inten-

sity is calculated by solving a global radiative transfer equation with an empirical model opacity due to hydrogen and helium, and a source function based on the observed UV luminosity function of quasars and star-forming galaxies. In the HM12 model, the gas is heated to $T_0 \sim 10^4$ K at redshift $z = 15$, where T_0 is the temperature at the mean gas density. The subsequent thermal evolution is calculated in RAMSES assuming photoionization equilibrium. As a result gas cools down to $T_0 \sim 7 \times 10^3$ K at $z \sim 6$ and then undergoes another episode of heating at $z \sim 2-4$ corresponding to helium reionization (Puchwein et al. 2015; Chardin et al. 2015). This has a corresponding effect on the structure of gas density due to pressure smoothing (Rorai et al. 2017; Pawlik et al. 2009). Gas density snapshots were taken from redshift $z = 100$ to $z = 2$ at 40 Myr intervals.

2.1 Radiative transfer

The radiative transfer calculations were performed in post-processing with ATON (Aubert & Teyssier 2008). ATON is a GPU-enabled radiative transfer code that implements a moment-based description of the radiative transfer equation. We employ a monochromatic radiation field, which assumes that all ionizing photons have an energy of 20.27 eV. This value corresponds to the mean energy of a 5×10^4 K blackbody spectrum, which is a close approximation to the spectral energy distribution of a stellar population with a Salpeter initial mass function with stellar masses in the range 1–100 M_\odot (Baek et al. 2009).

Haloes are identified in the base simulation using the HOP halo finder (Eisenstein & Hut 1998), with minimum halo mass consisting of 10 dark matter particles. Radiative transfer is started from the redshift at which the first halo collapses. In our fiducial simulation, ionizing sources are placed in dark matter haloes and assumed to emit continuously. As we discuss below, we also consider simulations in which ionizing sources are placed on the sides of the simulation box. The luminosities of ionizing sources are set assuming a linear scaling of the luminosity with halo mass (Iliev et al. 2006; Chardin et al. 2012, 2014). The normalization of this luminosity-mass relation is assumed to vary with redshift and is chosen so that the integrated comoving ionizing emissivity is similar to that of the HM12 uniform UV background model, but somewhat modified so as to obtain an improved match with the hydrogen photoionization rates inferred from Ly α forest data (Chardin et al. 2015).

We self-consistently follow recombination radiation and do not use the on-the-spot approximation (Rahmati et al. 2013): atoms recombine and radiate in an isotropic fashion, and are not directly reabsorbed by the freshly recombined hydrogen. Note that the impact of recombination radiation is likely to be underestimated in our simulations. Recombination radiation is expected to be emitted at a frequency close to the ionization threshold, where the hydrogen ionization cross-section $\sigma = 6.3 \times 10^{18}$ cm 2 is the highest, while our monochromatic frequency-averaged method tends to underestimate its absorption probability by assigning $\sigma = 1.6 \times 10^{18}$ cm 2 . The mean free path of these photons is thus larger than it should be, and a more accurate multi-frequency description would reduce the impact of recombinations. Moreover, we do not take into account the redshifting of the recombination photons by peculiar velocities of

Model	Box size (cMpc/h)	N_{grid}	Source model
L20N512	20	512^3	Halo
L20N512pp	20	512^3	Plane-parallel
L20N512fs	20	512^3	Restricted halo
L10N512pp	10	512^3	Plane-parallel
L10N512fs	10	512^3	Restricted halo

Table 1. Simulations used in this work: L20N512 is our fiducial simulation. The three source models are described in the text.

the emitters or the Hubble flow. In reality, recombination photons cannot travel to large cosmological distances without being redshifted to frequencies below the Lyman limit. Therefore, neglecting the cosmological redshifting of recombination radiation could in principle result in an overestimation of the photoionization rate on large scales. However, our simulation box is small enough that this is not a significant concern. The mean free path of redshifting is potentially a concern when the mean free path of photons exceeds the box size. This does not happen in our simulation until $z \lesssim 5$. Then, at these low redshifts, redshifting is not a concern because a uniform UV background is established.

2.2 Ionizing sources

Our fiducial simulation is performed in a cubical box 20 comoving Mpc/h on a side with periodic boundary conditions. In this model, we place sources of ionizing radiation at the locations of dark matter haloes, with a linear scaling of their luminosity with halo mass. The amplitude of this luminosity-mass relation is fixed by the HM12 model, as described above. For comparison, we also consider an equivalent simulation box in which plane-parallel radiation fronts are propagated in the three spatial directions (cf. Rahmati et al. 2013). This is achieved by placing radiation sources on the sides of the cubical box. We use 128 sources on each side. These sources have identical luminosities, which are chosen so that the total emissivity agrees with that in the HM12 model. A comparison of this plane-parallel model with our fiducial model allows us to isolate the effect of fluctuations in the photoionization rate due to sources. To check our results for numerical convergence, we also consider another simulation with a box size of 10 cMpc/h. The radiative transfer in our simulations is also performed in two ways: with local sources placed in dark matter haloes, and with plane-parallel radiation fronts.

The spatial resolution of our fiducial simulation is 39.1 ckpc/h, while the spatial resolution in the 10 cMpc/h box is 19 ckpc/h. At redshift $z = 10$, the minimum and maximum halo masses in our fiducial simulation are $M_{\text{min}} = 2 \times 10^8 M_{\odot}$ and $M_{\text{max}} = 5 \times 10^{10} M_{\odot}$. In the 10 cMpc/h box, the minimum and maximum halo masses at $z = 10$ are $3 \times 10^7 M_{\odot}$ and $10^{10} M_{\odot}$, respectively. However, when comparing the results from these simulations with our fiducial model in the case of local sources, we restrict the range of halo masses so that they are resolved by both boxes. This range is chosen to be between $M_{\text{min}} = 2 \times 10^8 M_{\odot}$ and $5 \times 10^9 M_{\odot}$. Haloes with mass outside this range do not host sources, even if present in the simulation box.

We consider five simulations as listed in Table 1, in which the fiducial simulation is labelled as L20N512. Simu-

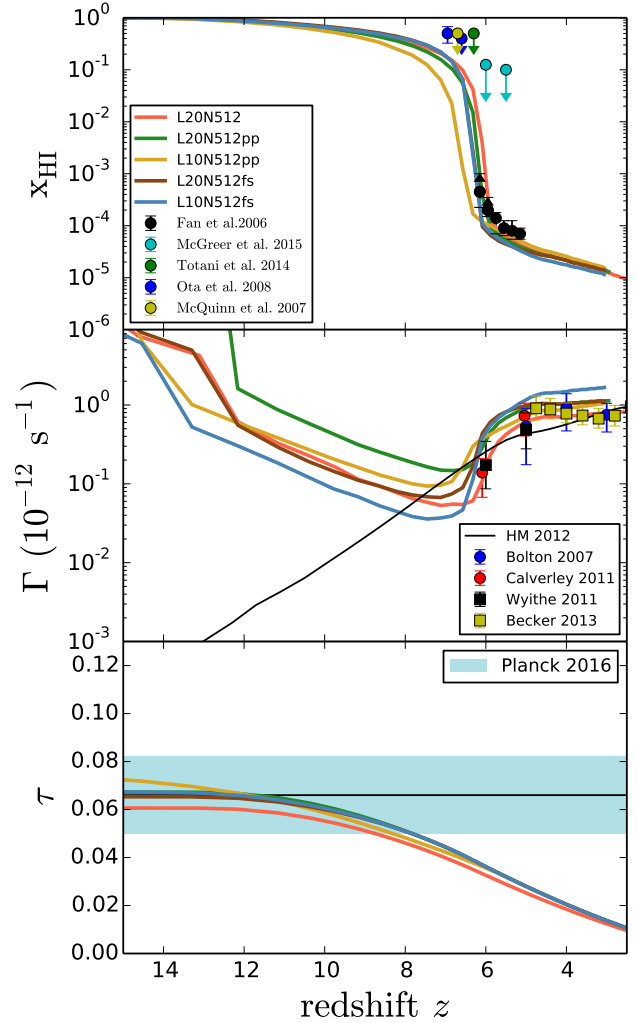


Figure 1. Calibration of the five simulations listed in Table 1. The top panel shows the evolution of the average neutral hydrogen fraction. Measurements shown are from Fan et al. (2006), McGreer et al. (2015), Totani et al. (2014), Ota et al. (2008), and McQuinn et al. (2007). The middle panel shows the evolution of the average photoionization rate compared with measurements by Bolton & Haehnelt (2007), Calverley et al. (2011), Wyithe & Bolton (2011) and Becker & Bolton (2013). The bottom panel shows the Thompson scattering optical depth, compared with the measurement from Planck Collaboration (2016).

lations with the plane-parallel source model have labels with the suffix ‘pp’, and simulations in which sources occupy a restricted range of halo masses are identified with labels that end in ‘fs’.

2.3 Calibration

As mentioned above, we use an ionizing emissivity that is close to that of the HM12 model in our simulations. Figure 1 shows the result. The top panel of Figure 1 shows the redshift evolution of the average neutral fraction in our different models. As all of our models are calibrated to the same HM12 reionization history, only small variations are seen be-

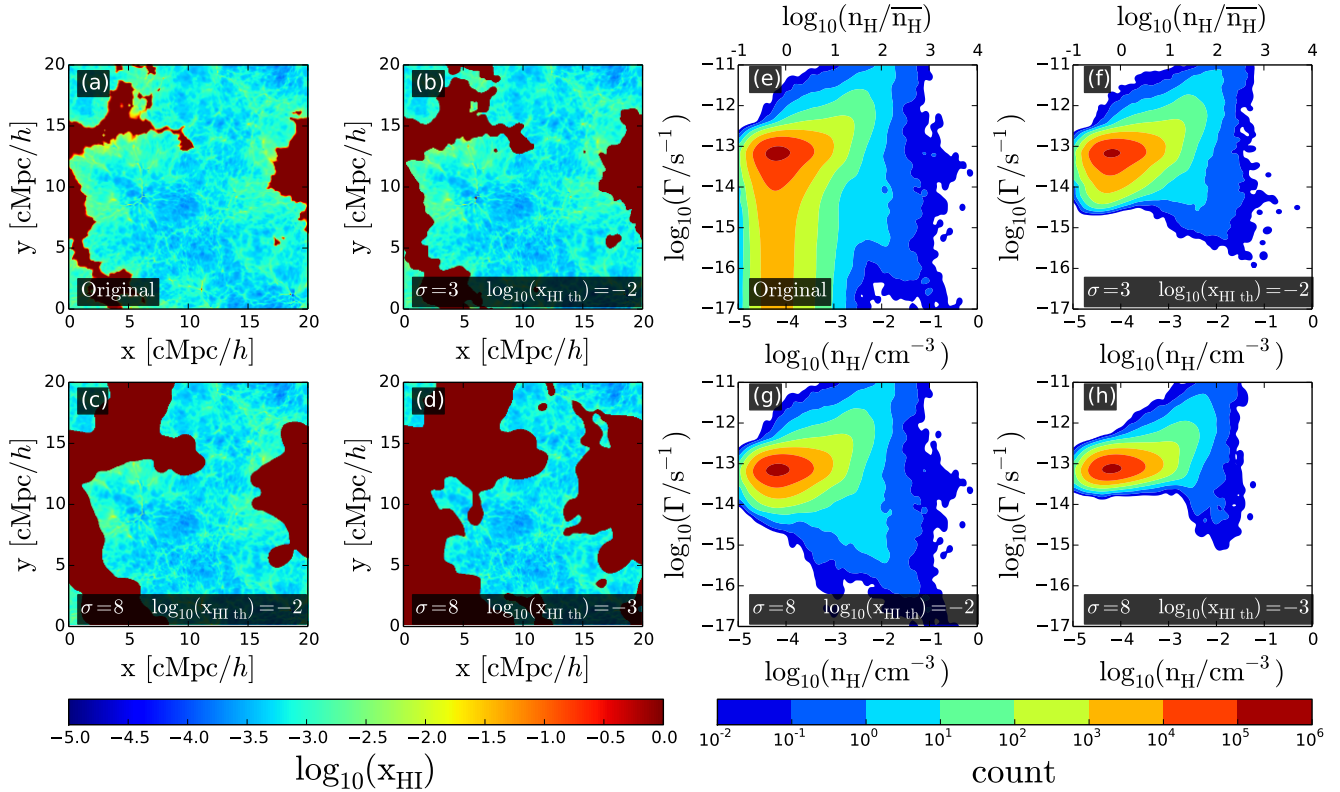


Figure 2. Isolation of self-shielded regions in our simulations. The four panels on the left show the neutral hydrogen distribution at $z = 7$ in our fiducial L20N512 simulation. The four panels on the right show the corresponding photoionization rate density distribution. The top left panel in each set shows the distributions before isolating the self-shielded regions. The other three panels show the result of convolving the spatial neutral hydrogen distribution with a Gaussian kernel of width σ and then, after convolution, discarding cells with a neutral hydrogen fraction less than $x_{\text{HI,th}}$.

tween the different models. All models lie close to the values of the neutral fraction derived from the Ly α forest data of Fan et al. (2006). This is also reflected in the bottom panel of Figure 1, which shows the electron scattering optical depth in the simulations. It is worth noting that simulations with the plane-parallel source model show an almost exactly similar reionization history compared to simulations with the fiducial source model. Adopting a tuned ionizing emissivity evolution with sources on the edges of the cosmological box can therefore mimic the simulations assuming the realistic positions of the sources. This similarity will allow us to compare directly the impact of the source location on the self-shielding properties of the gas both at high and low redshift.

The middle panel of Figure 1 shows the redshift evolution of the average hydrogen photoionization rate in ionized regions in our different models. The photoionization rate, $\langle \Gamma \rangle$, is averaged over the already ionized regions (i.e., regions with $x_{\text{HI}} \geq 0.5$). The evolution of the photoionization rate is consistent with observations in the post-overlap phase. Thus, regardless of ionizing source model considered, our fine tuning of the emissivity evolution with redshift results in a nearly identical reionization history. First, at high redshifts, the average photoionization rate drops with time due to geometric dilution, as the photons inside ionized re-

gions are consumed at the edges of ionized regions. Towards the end of reionization, the mean free path of ionizing photons rapidly increases when distinct ionized regions overlap, concomitantly increasing the photoionization rate. We note here that the agreement between the different models is not perfect, particularly at high redshifts. However, the post-reionization evolution of the average photoionization rate is always in good agreement with the observationally inferred photoionization rate at low redshifts. We therefore expect to see some variation between the different models at high redshifts. This may also lead to small differences in the characteristics of self-shielded regions in these simulations. We need to keep in mind those differences in the reionization histories when we interpret our results below. Finally, the bottom panel of Figure 1 shows that electron scattering optical depth in the simulations agrees with the Planck measurements (Planck Collaboration 2016).

3 THE SELF-SHIELDING OF HYDROGEN IN OUR SIMULATIONS

Panel (a) of Figure 2 shows the distribution of the neutral hydrogen fraction x_{HI} in a slice of thickness 39.1 ckpc/h at $z = 7$ in our fiducial simulation. The neutral hydrogen fraction is unity in regions of the simulation that are yet

to be reionized; in the ionized regions the neutral hydrogen fraction is generally low. However, in the ionized regions, x_{HI} varies with the total gas density between 10^{-5} and 0.1. This variation is partly due to fluctuations in the photoionization rate and partly due to self-shielding in high-density regions.

In order to study the neutral fraction in ionized regions, we need to isolate these regions in our simulation. This is difficult due to the complex morphology of these regions. A criterion that depends on the neutral hydrogen fraction at a location is unable to distinguish between a self-shielded cell within an ionized region and a cell in a region that is not yet ionized (the “neutral region” for short). In this work we disentangle the neutral and ionized regions in our simulation box by applying a neighbourhood criterion: a cell with high neutral fraction is deemed to lie in the neutral region if its neighbours also have a high neutral fraction.

The number of neighbours considered in this selection will obviously affect the result. We decide this by first selecting neighbours in a spherical region around a cell weighed, for simplicity, by a Gaussian. The width σ of the Gaussian and the threshold in the neutral hydrogen fraction, $x_{\text{HI,th}}$, are then chosen by visually comparing the resulting selection with the original slice from the simulation. Figure 2 shows results for a range of values of σ and $x_{\text{HI,th}}$. For a given value of σ , we consider if cells with neutral hydrogen fraction greater than $x_{\text{HI,th}}$ form contiguous neutral regions as opposed to isolated neutral cells in otherwise ionized regions. If the width of the Gaussian is too small, self-shielded regions are also marked as neutral. This is seen in Figure 2 in panel (b), which has $\sigma = 3$ cells. If the width is too large then parts of the neutral region are added to the ionized regions. Similar errors in identification occur if extreme values of $x_{\text{HI,th}}$ are used, as seen in panels (c) and (d). For the simulation and redshift shown in Figure 2, we use $\sigma = 8$ cells and $x_{\text{HI,th}} = 10^{-2}$, corresponding to panel (c) of Figure 2.

The four panels in the right half of Figure 2 show the photoionization rate distribution corresponding to the four panels in the left half. The average photoionization rate is $\sim 10^{-13} \text{ s}^{-1}$, consistent with the HM12 model. But, as seen in panel (e), the photoionization rate distribution in the simulation is characterized by high values ($\gtrsim 10^{-12} \text{ s}^{-1}$) close to sources in high density regions. The photoionization rate is the lowest in low density regions as some of these are not ionized yet ($\Gamma_{\text{HI}} = 0$). The effect of the selection procedure described above is seen in the other panels of Figure 2 (panels f, g, and h): selecting for ionized regions only leaves us with cells that have high photoionization rate at low densities. As we remove the neutral regions from Figure 2, a second branch starts to appear in the high density part of the plot. This branch is distinguished by a low photoionization rate. It is these cells that show the effect of self-shielding. However, in order to characterise them better we need to separate them from the high density, high photoionization rate cells located near sources of ionizing radiation.

In order to do this, we remove cells that contain sources from our analysis. We also remove a number of cells that are adjacent to the cells containing sources. This procedure is illustrated in Figure 3. Panel (a) of this figure shows the distribution of total gas density in our fiducial simulation at $z = 7$. The white circles in this panel show the locations of ionizing sources. These correspond to the centres of masses of dark matter haloes. The areas of the circles

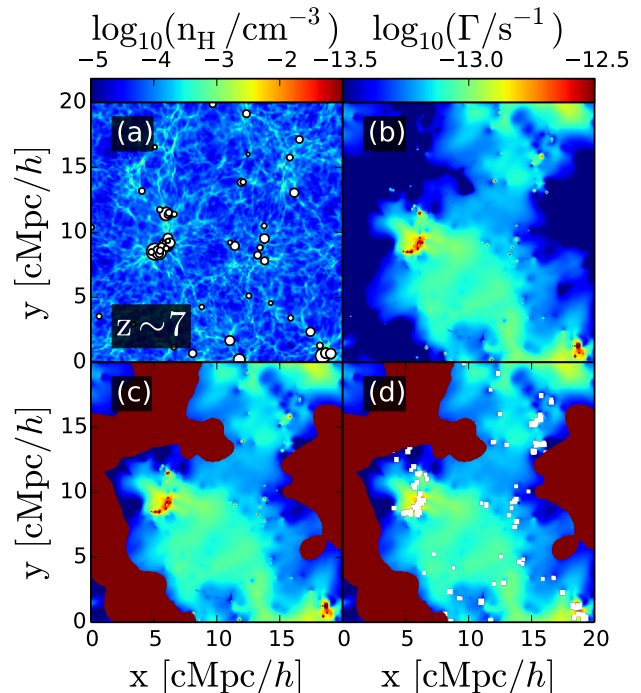


Figure 3. Illustration of the source exclusion process in simulations with local source model. Shown here is the fiducial L20N512 simulation. Panel (a) shows a slice through the hydrogen number density distribution in the simulation at $z = 7$. Sources are marked with white circles, with the circle radii scaling as the source luminosity. Panel (b) shows the photoionization rate distribution corresponding to panel (a). Panel (c) shows the photoionization rate distribution when the ionized regions are isolated by masking the neutral regions (brown) using the procedure described in Section 3. Panel (d) shows the masking of the sources.

are proportional to the source luminosity, and thus the halo mass. Panel (b) of Figure 3 shows the corresponding slice for the hydrogen photoionization rate. A comparison of these panels shows that the locations in the box with high photoionization rate ($\Gamma > 10^{-12} \text{ s}^{-1}$) correspond to the location of sources. Panel (c) shows the effect of removing the regions that are not reionized yet, following the procedure described above, while Panel (d) illustrates our masking of the high photoionization rate cells. We choose the number of cells to exclude based on the halo luminosity and resolution. The length of the cube excluded, centered around the halo location, depends on the halo mass as $r = a \log_{10}(M_{\text{halo}}) + b$. In our fiducial simulation, a cell size corresponds to the virial radius of a $3 \times 10^9 M_{\odot}$ halo at $z = 7$. Excluding a few cells around larger haloes will ensure that the high photoionization rate cells are completely removed from our analysis. We exclude a cubical region of about 8 to 14 cells on a side, depending on the halo mass.

The effect of removing sources on the photoionization rate distribution is illustrated in Figure 4 for various values of a and b . This figure also shows how we choose the values for a and b . Panel (a) of Figure 4 shows the photoionization rate density distribution for our fiducial simulation at $z = 7$, after isolating the ionized regions. We continue to

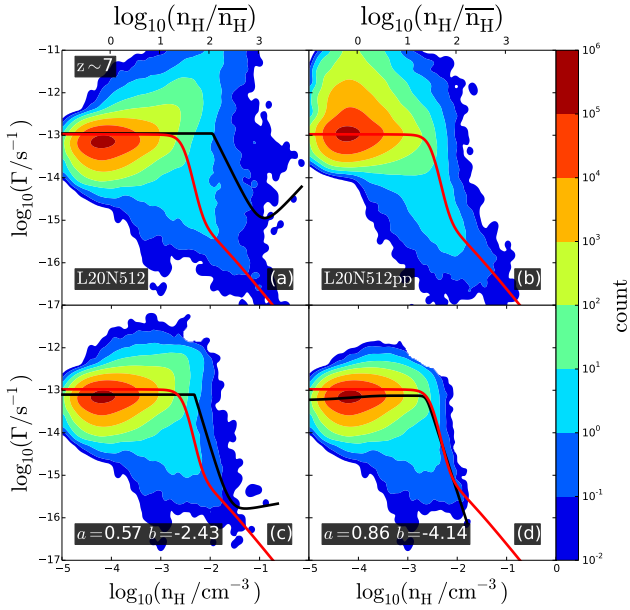


Figure 4. Effect of source exclusion on the photoionization rate density distribution. Panel (a) shows the distribution from the fiducial L20N512 simulation at $z = 7$. Panel (b) shows the photoionization rate density distribution from the L20N512pp simulation at the same redshift. A comparison of these two panels shows that the top right part of the distribution in Panel (a) is affected by enhanced photoionization rate near ionizing sources. Panels (c) and (d) show how this is corrected by masking these sources by following the procedure illustrated in Figure 3. Cubical regions around source centres are masked, with the length of the cube taken to be $r = a \log_{10}(M_{\text{halo}}) + b$. Panels (c) and (d) show the result for two different values of the parameters a and b . The red curve in panel (b) shows the median photoionization rate; this curve is reproduced in panels (c) and (d). The black curves in all panels show the respective median photoionization rates. We choose values of the parameters a and b corresponding to panel (d) so that the median photoionization rate agrees with that in the plane-parallel case.

see regions with high density and high photoionization rate. These regions can also be identified by contrasting panel (a) with panel (b), which shows the photoionization rate density distribution in the L20N512pp simulation. Sources in this simulation are located on the face of the box; as a result, they are not correlated with density, and cells with enhanced photoionization rate then move closer to the mean density. Panels (c) and (d) show the effect of removing cells containing sources from the fiducial simulation, for different values of a and b . As expected, cells with high photoionization rate vanish when we exclude the sources and their neighbouring cells. The curves in panels (b), (c), and (d) show the *median* photoionization rates as a function of density. The red curves in panels (c) and (d) show the median curve from panel (b) for easy comparison, while black curves in panels (c) and (d) show the medians from the respective photoionization rate distributions. At high densities, the photoionisation rate distribution in panel (a) is bimodal; we choose values of a and b that completely remove cells belonging to the high photoionization rate branch. At the end of this procedure, only the self-shielded cells, which lie in ionized regions, remain.

When this happens, the median photoionization rate agrees with that in the corresponding plane-parallel simulation, as seen in panel (d). We have chosen $a = 0.86$ and $b = -4.14$ for the fiducial simulation at $z = 7$. We identify the values of a and b for each of our simulations at all redshifts separately. In practice, the values are not very different from those for the fiducial simulation.

Figure 5 shows the photoionization rate density distributions from redshift $z = 3$ to $z = 10$ after the neutral regions are removed following the procedure described above. Note that cells located near ionizing sources have not been masked yet. In Figure 5, we show results from the L10N512fs simulation instead of our fiducial L20N512 simulation, as the former simulation better illustrates the behaviour of the photoionization rate at high densities, due to its higher resolution. As we will discuss below, the results are nearly identical in the two simulations. The average photoionization rate follows the evolution seen in Figure 1: there is little evolution from $z = 10$ to $z = 7$ and then a jump by an order of magnitude from $\Gamma \sim 10^{-13} \text{ s}^{-1}$ to $\Gamma \sim 10^{-12} \text{ s}^{-1}$ at $z = 6$. The density dependence of the photoionization rate has a characteristic shape that remains essentially unchanged throughout reionization: low density regions have high photoionization rates and high density regions (that are not close to ionizing sources) have low photoionization rates. This shape is caused by the shielding. As a uniform photoionization rate background gets established after the completion of reionization, the photoionization rate distribution in Figure 5 narrows.

The photoionization rate distribution shown in Figure 5 can now be used to understand self-shielding in our simulations. We find that, at all redshifts studied here, the photoionization rate has a background value at low densities that does not depend on the gas density. The spread around the background value is quite small at low redshifts but is larger at high redshifts, before individual ionized regions have percolated. At high densities ($n_{\text{H}} \gtrsim 5 \times 10^{-3} \text{ cm}^{-3}$), the photoionization rate drops below its background value due to self-shielding. At even higher densities ($n_{\text{H}} \gtrsim 5 \times 10^{-2} \text{ cm}^{-3}$), the photoionization rate increases further, due to recombination radiation. This causes the photoionization rate density curve to flatten at very high densities.

We find that the photoionization rate distribution is described very well by the fitting function introduced by Rahmati et al. (2013),

$$\frac{\Gamma}{\langle \Gamma \rangle_{\text{HII}}} = (1 - f) \left[1 + \left(\frac{n_{\text{H}}}{n_0} \right)^{\beta} \right]^{\alpha_1} + f \left[1 + \frac{n_{\text{H}}}{n_0} \right]^{\alpha_2}. \quad (1)$$

In this fitting function, the parameter n_0 describes the characteristic density at which self-shielding occurs. The parameters β and α_1 describe the slope of the photoionization rate density curve caused by self-shielding, while the parameters f and α_2 describe the enhanced slope of the photoionization rate density curve at the highest densities. We fit this form to the photoionization rate distributions of Figure 5, after masking the sources following the procedure described above. This fit is illustrated by the solid red curves in Figure 5. Figure 6 shows the corresponding fits in the plane-parallel source model (L10N512pp). The black solid curves show the result from comparable simulations by Rahmati et al. (2013) at redshifts $z < 6$. Rahmati et al. (2013) noted that the parameters in Equation (1) do not seem to evolve significantly between redshifts $z = 1$ and $z = 6$ in their simula-

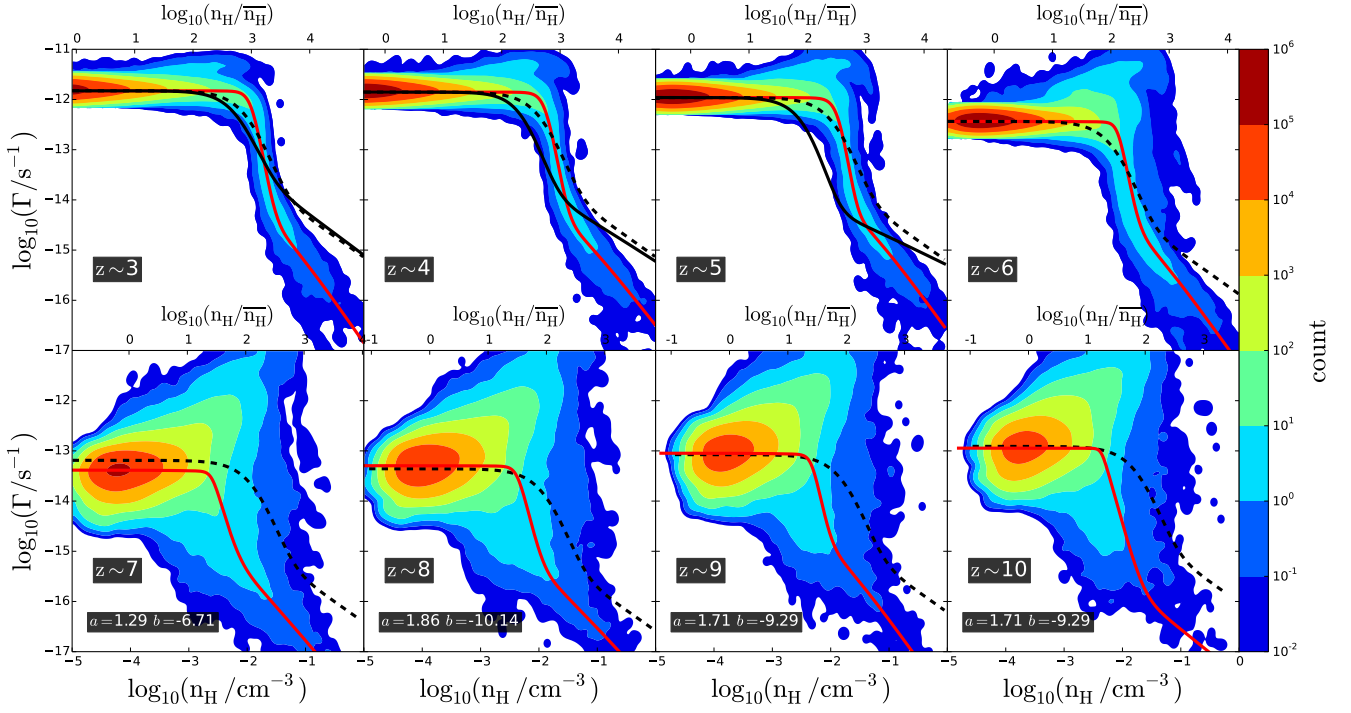


Figure 5. The photoionization rate density distribution at various redshifts from the L10N512fs simulation. In each panel, the red curve shows the best-fit curve of the form given by Equation 1. (Note that the curve is fit after masking regions near ionizing sources, as described in the text. However the masked regions are still shown in the figure.) The black solid curves show the fits presented by Rahmati et al. (2013) at $z < 6$, while the black dashed curve shows their ‘average’ fit.

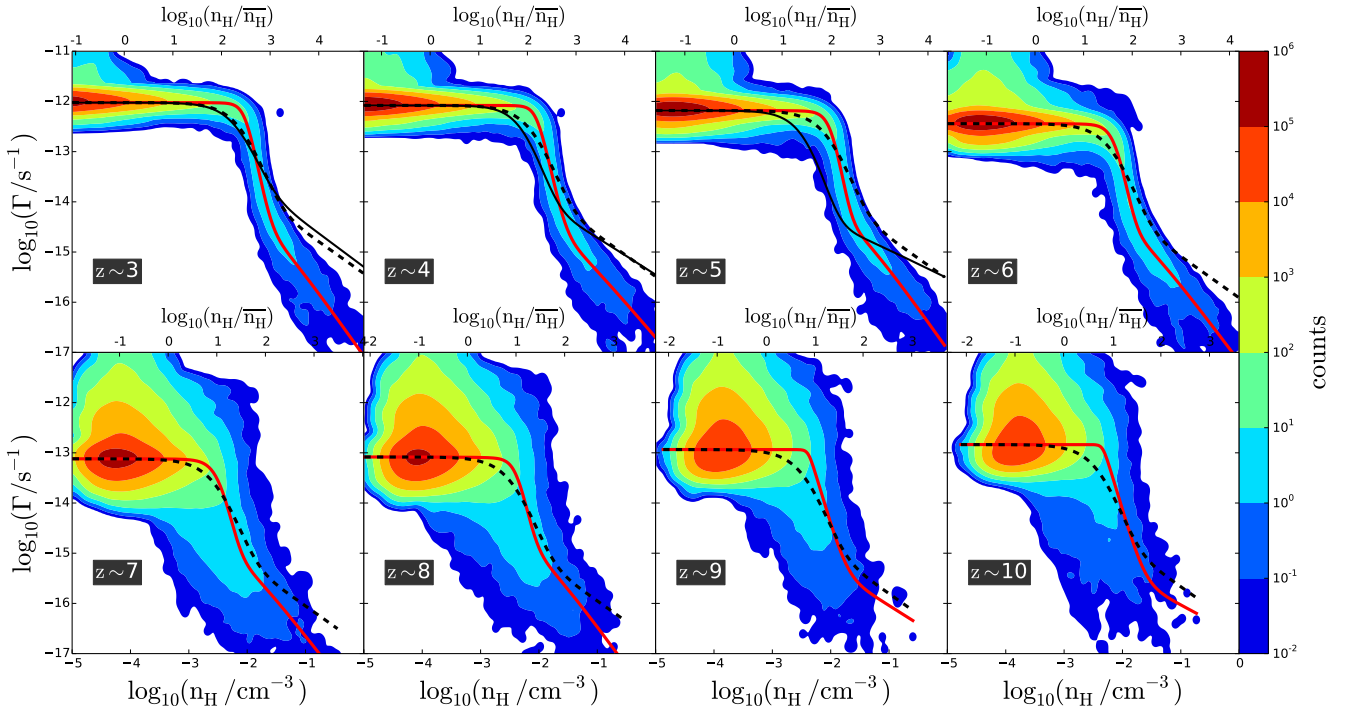


Figure 6. The photoionization rate density distribution at various redshifts from the L10N512pp simulation. The various curves shown are the same as in Figure 5.

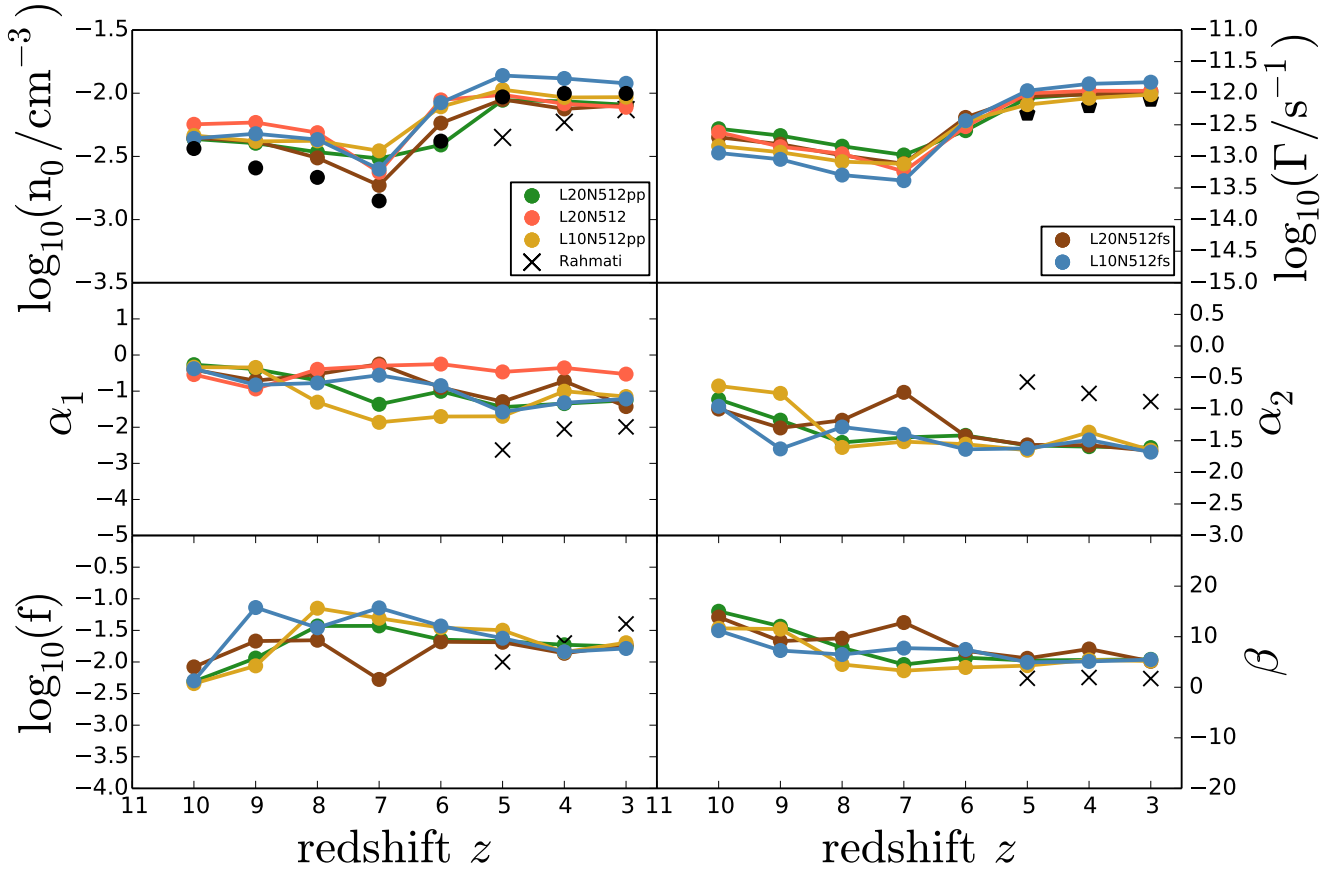


Figure 7. Evolution of the volume-averaged hydrogen photoionization rate in ionized regions, and of the five parameters of Equation 1 in all five simulations considered in this paper. Black crosses show parameter values from [Rahmati et al. \(2013\)](#). In the photoionization rate panel, the black symbols show the photoionization rate inferred from the fits provided by [Rahmati et al. \(2013\)](#), by using Equation 2. Similarly, black filled circles in the n_0 panel, show the self-shielding density given by Equation 2 for the fiducial simulation. As discussed in the text, the L20N512 simulation does not constrain the slope parameters very well. Therefore, this simulation is only shown in three of the six panels.

tions. Therefore, they put forward a single set of parameter values to describe the photoionization rate density curve in this redshift range. The black dashed curve in all panels of Figures 5 and 6 shows this “average” curve.

The photoionization rate distributions in Figures 5 and 6 have several interesting features. In both cases, at all redshifts, Equation (1) describes the distributions very well. In the L10N512fs model (Figure 5), in which ionizing sources are placed at the locations of haloes, there is an enhancement in the photoionization rate at high densities due to the presence of sources in this regions, as discussed above. In the plane-parallel L10N512pp simulation, this enhancement is no longer seen; instead, at lower densities, there is a spread in the photoionization rate around the background values. This spread is due to the enhancement of the photoionization rate in cells that are close to the sides of the simulation box, where the “sources” of the plane-parallel fronts are located. As most of the cells have low densities (close to the mean) the spread in the photoionization rate also moves to these densities. The difference between the fiducial and the plane-parallel models is also reflected at the high density end

of this plot. We find that the high density part is better sampled in the plane-parallel simulation than in the fiducial simulation because in the latter, many of these cells are transferred to the high photoionization rate part of the plot due to the presence of ionizing sources in them. This is reflected in the relatively poor fits at high densities in the L10N512fs simulation, compared to the L10N512pp simulation. Note that in all of our simulations, the high density cells are also affected by star formation. Finally, our simulations corroborate the findings of [Rahmati et al. \(2013\)](#) by also showing very little evolution in self-shielding across redshifts, even at redshifts before reionization. Nonetheless, there are differences between our best-fit model and that of [Rahmati et al. \(2013\)](#): the characteristic slope of the self-shielding transition is much steeper in both our restricted-halo and plane-parallel simulations. As we discuss in greater detail below, this difference arises due to a combination of three reasons: (a) difference in the radiative transfer method, (b) star formation, and (c) recombination radiation. [Rahmati et al. \(2013\)](#) highlight the role of different radiative transfer algorithms by noting a similar difference between their

results and those from ray-tracing radiative transfer simulations by [Altay et al. \(2011\)](#). We have already mentioned that the star formation prescription used in our simulations may deplete regions with high gas density, thereby affecting the results shown in Figures 5 and 6. Finally, the effect of recombinations is likely underestimated in our simulations due to their monochromatic nature, as discussed in Section 2.1. The temperature evolution in our simulations is unlikely to have an effect on the photoionisation rate distribution due to the small pressure smoothing scale at these redshifts ([Kulkarni et al. 2015](#)).

The redshift evolution of the parameters in Equation (1) is summarised in Figure 7 for all five of our simulations. Also shown in the top right panel of this figure is the evolution of the volume-averaged photoionization rate in ionized regions. Red points in Figure 7 show results from our fiducial simulations for redshifts $z = 3$ –10. All simulations agree with each other to a reasonable degree, particularly in the evolution of the characteristic self-shielding density n_0 . The black crosses in Figure 7 show the corresponding values from [Rahmati et al. \(2013\)](#) for $z < 6$. We find that the self-shielding density n_0 stays roughly constant at $n_0 \sim 10^{-2} \text{ cm}^{-3}$ at post-reionization redshifts ($z < 6$). This density corresponds to overdensities of about 100. At higher redshifts, the self-shielding density is lower, $n_0 \sim 10^{-3} \text{ cm}^{-3}$, which corresponds to overdensities of about 10. It is apparent from comparing the top two panels of Figure 7 that the characteristic self-shielding density n_0 follows the evolution in the photoionization rate at all redshifts. As discussed above, and evidenced by Figures 5 and 6, the self-shielding density in our simulations is close to that in the simulations of [Rahmati et al. \(2013\)](#). The self-shielding density can be written as a function of the photoionization rate as ([Schaye 2001](#); [Furlanetto et al. 2005](#); [Rahmati et al. 2013](#)),

$$n_0 \sim 6.73 \times 10^{-3} \text{ cm}^{-3} \left(\frac{\sigma_{\nu\text{HI}}}{2.49 \times 10^{-18} \text{ cm}^2} \right)^{-2/3} \times T_4^{0.17} \Gamma_{-12}^{2/3} \left(\frac{f_g}{0.17} \right)^{-1/3}, \quad (2)$$

where $T_4 = T/10^4$, $\Gamma_{-12} = \Gamma/10^{-12} \text{ s}^{-1}$, and $f_g = \Omega_b/\Omega_m$ is the cosmic baryon fraction. This relation assumes absorbers with temperature $T \sim 10^4 \text{ K}$, column density $N_{\text{HI}} \sim 1/\sigma$, and a typical size given by the Jeans scale. The black points in the top left panel of Figure 7 show the n_0 derived from our volume-averaged photoionization rate from ionized regions using Equation (2) for the fiducial simulation. We find that Equation (2) describes the evolution in n_0 reasonably well. At low redshifts ($z < 6$) the agreement is very good. At high redshifts there is a constant offset due to the difference in the cell selection for the photoionization rate and self-shielding density. The average values of parameters shown in Figure 7 are presented in Appendix A as a function of redshift. These should be useful for use in simulations without radiative transfer that rely on approximate models for self-shielding.

The slopes of the photoionization rate density distribution also agree quite well between various simulations. The fiducial simulation (L20N512) is unable to resolve the highest density part of the distribution very well, partly due to the low spatial resolution and partly because the sources in this simulation occupy a wide dynamic range in halo mass. Therefore, Figure 7 only shows one of the slopes, α_1 , from

this simulation. There are also differences between the slopes in our simulations and those of [Rahmati et al. \(2013\)](#) at post-reionization redshifts. As discussed by [Rahmati et al. \(2013\)](#), this is partly due to the difference in the radiative transfer methods, but also due to the difference in the way recombination radiation is treated.

4 DISCUSSION

The self-shielding of intergalactic hydrogen described in the previous section is potentially sensitive to several assumptions made in our simulations. We now discuss some of the more important of these.

Figure 7 highlights the agreement between all of our simulations, quantified using the fitting function in Equation (1). As discussed above, as in the fiducial simulation, the self-shielding density n_0 stays roughly constant at 10^{-2} cm^{-3} at post-reionization redshifts ($z < 6$) and tracks the photoionization rate evolution at higher redshifts. The self-shielding density agrees between the simulations to within a factor of 2. This level of discrepancy is completely explained by the differences in the photoionization rate in these simulations, as seen in Figure 1. A similar level of agreement is seen in the parameters β and α_1 , which describe the characteristic slope of the photoionization rate density relation caused by self-shielding. There is significant improvement in the parameters, f and α_2 , which predominantly describe the modification of the slope of the photoionization rate density relation at high densities due to recombination radiation. This is because the high densities are much better resolved in the higher resolution simulations than in the fiducial simulation ([Rahmati et al. 2013](#)).

It has been noted in the literature that self-shielding in simulations can also be affected by the radiative transfer method used. In this paper we have used a moment-based algorithm of radiative transfer, as implemented in ATON (see Section 2.1). We have performed monochromatic radiative transfer but self-consistently include the recombination radiation. We do not use the on-the-spot approximation. In contrast, for example, [Rahmati et al. \(2013\)](#) used the TRAPHIC code ([Pawlik & Schaye 2008](#)) in their work, where radiative transfer is implemented by tracing photon packets. This technique is very different from the moment-based method used in the present paper. [Altay et al. \(2011\)](#) used a ray-tracing radiative transfer algorithm in the OWLS simulations. These authors ignore recombination radiation. [Rahmati et al. \(2013\)](#) note that self-shielding in OWLS is somewhat different from their simulation at least at post-reionization redshifts, although overall the agreement is good. The characteristic slope of the photoionization rate density relation is somewhat steeper in the ray tracing case as compared to the photon packet method. This could partly be a resolution effect and partly be due to inaccuracies in calculating the absorption of UV photons at large scales in the ray-tracing codes. In Figure 8, we compare our result from the fiducial 20 cMpc/ h box with a similar simulation that uses the moment-based radiative transfer as implemented by [Bauer et al. \(2015\)](#). This simulation is performed on a 256^3 grid in a 10 cMpc/ h box so that it has the same spatial resolution as our fiducial simulation. The radiative transfer algorithm used by [Bauer et al. \(2015\)](#) uses the

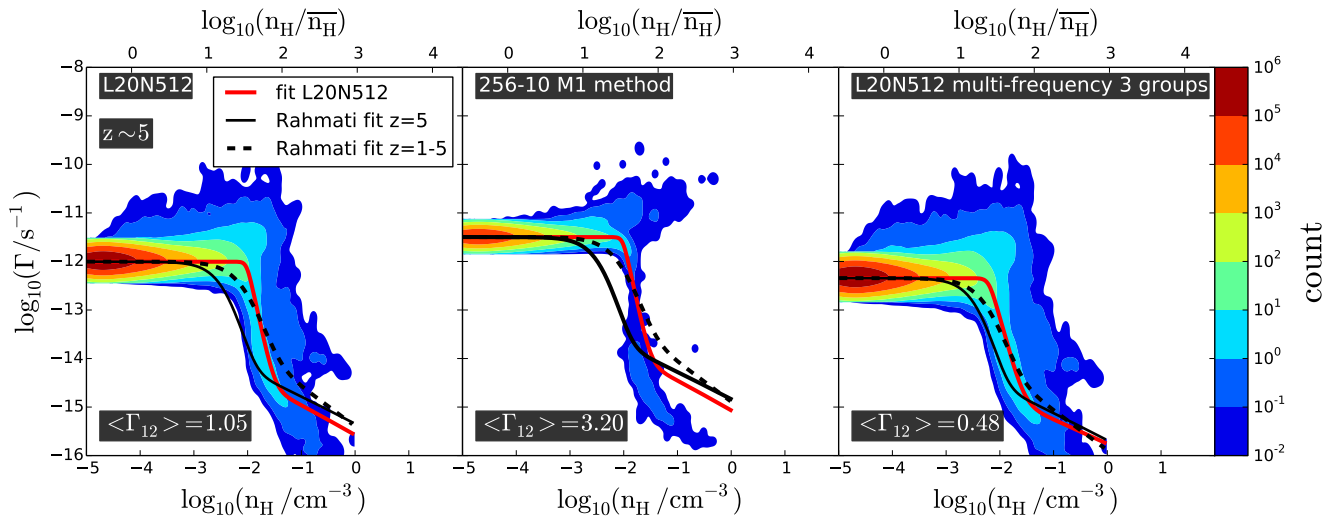


Figure 8. Comparison of our results with those from two other simulations. The left panel shows the photoionization rate distribution at $z = 5$ from our L20N512 simulation. The middle panel shows the photoionization rate distribution at the same redshift when the radiative transfer calculation is performed with the same density and source fields but using the moment-based implementation by [Bauer et al. \(2015\)](#). The right panel shows results from a multi-frequency simulation using three frequency bins. In all three panels, the red curve shows the best-fit curve of the form given by Equation 1 from left panel. The solid and dashed black curves in all three panels show two photoionization rate distribution fits from [Rahmati et al. \(2013\)](#).

M1 closure similar to our radiative transfer method. Both of these simulations are at redshift $z = 5$. They use similar density and source fields, and are calibrated in similar way. The solid red curve in Figure 8 shows the fit to the photoionization rate density distribution from the fiducial L20N512 simulation. But the middle panel of Figure 8 shows that this provides a good description also of the results from a different radiative transfer implementation. It is also interesting that both simulations have steeper characteristic slopes as compared to the results of [Rahmati et al. \(2013\)](#): the dashed black curve shows the average fit from their work while the solid black curve shows their fit at redshift $z = 5$. Both curves have shallower characteristic slopes that in our simulations at this redshift. This suggests that the shallower slopes of [Rahmati et al. \(2013\)](#) could be a result of limited resolution.

The third panel of Figure 8 explores the effect of monochromaticity in our simulations. It shows the photoionization rate density distribution at redshift $z = 5$ from a multi-frequency counterpart of our fiducial simulation. This simulation uses three photon energy bins at 17.87 eV, 30.23 eV, and 59.38 eV, but otherwise has identical properties as our fiducial simulation. Figure 8 shows that the resultant picture of self-shielding emerging from this multi-frequency simulation is remarkably similar to that in our monochromatic simulation. The red curve in this panel shows our best-fit model from our L20N512 simulation at $z = 5$. The self-shielding density and the characteristic slope are in agreement with the multi-frequency simulation. (The normalization of the curve has been adjusted to match with the somewhat different value of the average photoionization rate, $\langle \Gamma \rangle_{\text{HII}}$, which has values of 10^{-12} s^{-1} , $3 \times 10^{-12} \text{ s}^{-1}$, and $6 \times 10^{-13} \text{ s}^{-1}$, in the three simulations shown in Figure 8, respectively.) The red curve, which describes the simulation

in the left panel of Figure 8 also provides a good description of the photoionisation rate distribution in the central and right panels of this figure. The best fit parameters for the three simulations agree to within 10%.

Finally, in Figure 9, we show the evolution of the clumping factor, the mass and volume fractions contained in the self-shielded regions, and the average number of recombinations per hydrogen atom in our simulations. The clumping factor is defined here as $C = \langle n_{\text{HII}}^2 \rangle / \langle n_{\text{HII}} \rangle^2$ and is evaluated only in ionized regions. As expected the clumping factor grows with time as nonlinear structure develops. During the epoch of reionization ($z \sim 6-10$), the clumping factor is low, about 2–3. This is in agreement with previous results from [Pawlik et al. \(2009\)](#) and [Iliev et al. \(2006\)](#). Further, as the middle panel of Figure 9 shows, the self-shielded systems occupy a very small ($< 0.1\%$) fraction of the volume. The fractional mass content is relatively larger, about 1% at $z \sim 6$, decreasing to 0.1% up to $z \sim 10$. The decrease in the mass fraction towards high redshifts is due to the increase in the photoionization rate in high density regions. Note that the fiducial simulation, L20N512, shows considerably different behaviour in the evolution of the mass and volume fractions and the mean number of recombinations per hydrogen atom, due to the poor resolution of this simulation in this regime, as discussed above.

A better measure of the effect of clumping on how reionization proceeds, is the average number of recombinations per hydrogen atom in ionized regions, defined as

$$\bar{n}_{\text{rec}}(t) = \int_0^t dt \alpha_{\text{B}}(t) \left\langle \frac{n_{\text{HII}}(t)^2}{n_{\text{H}}(t)} \right\rangle \quad (3)$$

where α_{B} is the case-B recombination rate of ionized hydrogen, which evolves due to the evolution of gas temperature, and the average is over ionized regions. There is relatively

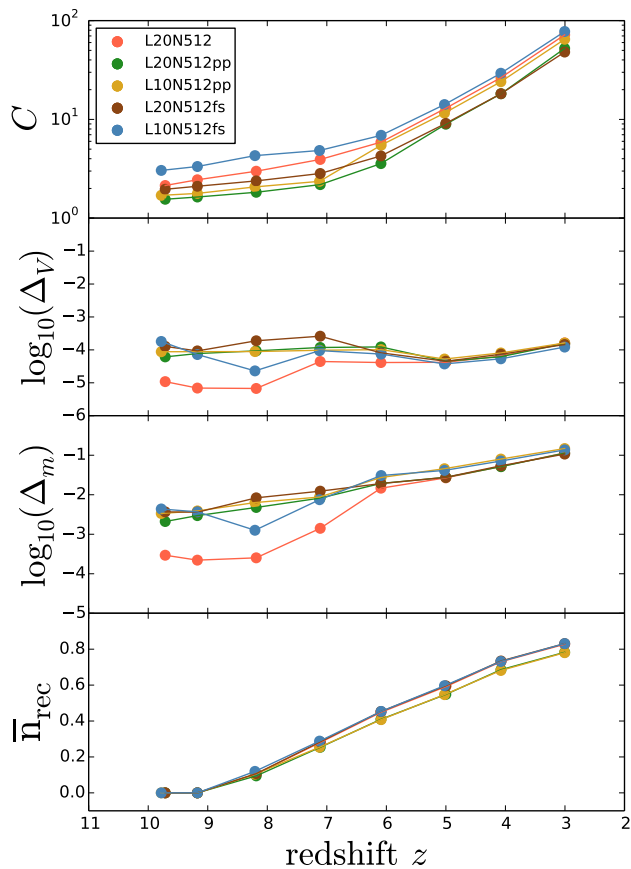


Figure 9. Evolution of the clumping factor, the volume and mass fraction of self-shielded regions, and the mean number of recombinations per hydrogen atom in the five simulations presented in this paper.

little difference between the mean number of recombinations in various simulations, as most differences are at high redshifts where the contribution to the integral in Equation (3) is small. The value of \bar{n}_{rec} is somewhat smaller than previous studies Iliiev et al. (2006). This is partly due to enhanced self-shielding in our simulations due to relatively high resolution. This reduces the number of high density ionized regions, thereby reducing the number of recombinations.

5 CONCLUSIONS

We have used here full radiative transfer simulations of the epoch of hydrogen reionization carefully calibrated with Ly α forest data to study the self-shielding of hydrogen during and after reionization. We find that in spite of large fluctuations in the photoionization rate during reionization, the characteristic density above which self-shielding is important follows the evolution of the average photoionization rate in a manner similar to that in the post-reionization Universe. This results in similar typical values for the characteristic self-shielding density, of 10^2 – 10^3 cm $^{-3}$ for a wide range of redshifts from $z = 10$ to $z = 2$. This corresponds to overdensities of ~ 100 in the post-reionization Universe,

but more like ~ 10 during reionization, reflecting the fact that during reionization photoionization rates are typically low enough that the filaments in the cosmic web are often self-shielded.

We have shown our findings to be robust against various assumptions made in our study and have shown that our inferred values of the self-shielding density have converged with respect to numerical resolution in our simulation. The detailed properties of the ionizing sources are not critically important as long as they result in a similar evolution of the photoionization rate and ionized gas fraction. The results from our mono-frequency radiative transfer simulations are in good agreement with those from equivalent multi-frequency radiative transfer simulations. Our results are also in good overall agreement with previous studies of the post-reionization IGM (Rahmati et al. 2013), but with a steeper slope of the self-shielding transition.

To obtain our results we have developed a method to efficiently isolate the ionized regions in our simulations, which should have wider applications in the study of reionization simulations and for the analysis of future datasets that will yield a three-dimensional tomographic view of the epoch of reionization by measuring the brightness of the 21 cm line from the IGM.

Although self-shielded regions occupy a very small fraction of the cosmological volume, they nevertheless contain about 0.1–1% of the total hydrogen mass during the epoch of reionization in our simulation. This has an effect on the recombination rate of hydrogen, which can be quantified by the average number of recombinations per hydrogen atom. The typical value of this quantity in our simulations during reionization is less than 0.4, slightly smaller than previous studies. Self-shielded regions of neutral hydrogen are known to critically affect the visibility of Ly α emitters during the epoch of reionization as well as the clustering properties of the 21 cm signal on large scales. Modelling self-shielding accurately is thus important. We have provided parameter values at high redshifts for the fitting formula proposed by Rahmati et al. (2013) for the self-shielding transition for use in simulations without radiative transfer that rely on approximate models of self-shielding.

ACKNOWLEDGMENTS

We thank James Bolton, Tirthankar Roy Choudhury, Harley Katz, Laura Keating, and Ewald Puchwein for helpful discussions. This work was supported by the ERC Advanced Grant 320596 “The Emergence of Structure during the epoch of Reionization”. The RAMSES simulations presented in this paper were performed on the COSMOS Shared Memory system at DAMTP, University of Cambridge operated on behalf of the STFC DiRAC HPC Facility. This equipment is funded by BIS National E-infrastructure capital grant ST/J005673/1 and STFC grants ST/H008586/1, ST/K00333X/1. The ATON radiative transfer simulations in this work were performed using the Wilkes GPU cluster at the University of Cambridge High Performance Computing Service (<http://www.hpc.cam.ac.uk/>), provided by Dell Inc., NVIDIA and Mellanox, and part funded by STFC with industrial sponsorship from Rolls Royce and Mitsubishi Heavy Industries.

REFERENCES

- Altay G., Theuns T., Schaye J., Crighton N. H. M., Dalla Vecchia C., 2011, *ApJ*, **737**, L37
- Altay G., Theuns T., Schaye J., Booth C. M., Dalla Vecchia C., 2013, *MNRAS*, **436**, 2689
- Anderson L., Governato F., Karcher M., Quinn T., Wadsley J., 2016, preprint, ([arXiv:1606.05352](https://arxiv.org/abs/1606.05352))
- Aubert D., Teyssier R., 2008, *MNRAS*, **387**, 295
- Baek S., Di Matteo P., Semelin B., Combes F., Revaz Y., 2009, *A&A*, **495**, 389
- Barkana R., Loeb A., 2001, *Phys. Rep.*, **349**, 125
- Barnett R., Warren S. J., Becker G. D., Mortlock D. J., Hewett P. C., McMahon R. G., Simpson C., Venemans B. P., 2017, preprint, ([arXiv:1702.03687](https://arxiv.org/abs/1702.03687))
- Bauer A., Springel V., Vogelsberger M., Genel S., Torrey P., Sijacki D., Nelson D., Hernquist L., 2015, *MNRAS*, **453**, 3593
- Becker G. D., Bolton J. S., 2013, *MNRAS*, **436**, 1023
- Bolton J. S., Haehnelt M. G., 2007, *MNRAS*, **382**, 325
- Bolton J. S., Haehnelt M. G., 2013, *MNRAS*, **429**, 1695
- Calverley A. P., Becker G. D., Haehnelt M. G., Bolton J. S., 2011, *MNRAS*, **412**, 2543
- Chardin J., Aubert D., Ocvirk P., 2012, *A&A*, **548**, A9
- Chardin J., Aubert D., Ocvirk P., 2014, *A&A*, **568**, A52
- Chardin J., Haehnelt M. G., Aubert D., Puchwein E., 2015, *MNRAS*, **453**, 2943
- Chardin J., Puchwein E., Haehnelt M. G., 2017, *MNRAS*, **465**, 3429
- Choudhury T. R., Ferrara A., 2005, *MNRAS*, **361**, 577
- Choudhury T. R., Haehnelt M. G., Regan J., 2009, *MNRAS*, **394**, 960
- Choudhury T. R., Puchwein E., Haehnelt M. G., Bolton J. S., 2015, *MNRAS*, **452**, 261
- Eisenstein D. J., Hut P., 1998, *ApJ*, **498**, 137
- Fan X., et al., 2006, *AJ*, **132**, 117
- Furlanetto S. R., Oh S. P., 2005, *MNRAS*, **363**, 1031
- Furlanetto S. R., Schaye J., Springel V., Hernquist L., 2005, *ApJ*, **622**, 7
- Gnedin N. Y., 2000, *ApJ*, **535**, 530
- Haardt F., Madau P., 2012, *ApJ*, **746**, 125
- Iliev I. T., Mellema G., Pen U., Merz H., Shapiro P. R., Alvarez M. A., 2006, *MNRAS*, **369**, 1625
- Kaurov A. A., Gnedin N. Y., 2013, *ApJ*, **771**, 35
- Kaurov A. A., Gnedin N. Y., 2014, *ApJ*, **787**, 146
- Keating L. C., Haehnelt M. G., Cantalupo S., Puchwein E., 2015, *MNRAS*, **454**, 681
- Kulkarni G., Hennawi J. F., Oñorbe J., Rorai A., Springel V., 2015, *ApJ*, **812**, 30
- Kulkarni G., Choudhury T. R., Puchwein E., Haehnelt M. G., 2016, *MNRAS*, **463**, 2583
- McGreer I. D., Mesinger A., D’Odorico V., 2015, *MNRAS*, **447**, 499
- McQuinn M., Hernquist L., Zaldarriaga M., Dutta S., 2007, *MNRAS*, **381**, 75
- McQuinn M., Oh S. P., Faucher-Giguère C.-A., 2011, *ApJ*, **743**, 82
- Mesinger A., Aykutaalp A., Vanzella E., Pentericci L., Ferrara A., Dijkstra M., 2015, *MNRAS*, **446**, 566
- Miralda-Escudé J., Haehnelt M., Rees M. J., 2000, *ApJ*, **530**, 1
- Mitra S., Choudhury T. R., Ferrara A., 2015, *MNRAS*, **454**, L76
- Mutch S. J., Geil P. M., Poole G. B., Angel P. W., Duffy A. R., Mesinger A., Wyithe J. S. B., 2016, *MNRAS*, **462**, 250
- Ota K., et al., 2008, *ApJ*, **677**, 12
- Pawlik A. H., Schaye J., 2008, *MNRAS*, **389**, 651
- Pawlik A. H., Schaye J., van Scherpenzeel E., 2009, *MNRAS*, **394**, 1812
- Planck Collaboration 2016, *A&A*, **596**, A108
- Planck Collaboration et al., 2014, *A&A*, **571**, A16
- Puchwein E., Bolton J. S., Haehnelt M. G., Madau P., Becker G. D., Haardt F., 2015, *MNRAS* accepted, ArXiv e-prints 1410.1531,
- Rahmati A., Pawlik A. H., Raičević M., Schaye J., 2013, *MNRAS*, **430**, 2427
- Robertson B. E., Ellis R. S., Furlanetto S. R., Dunlop J. S., 2015, *ApJ*, **802**, L19
- Rorai A., et al., 2017, preprint, ([arXiv:1704.08366](https://arxiv.org/abs/1704.08366))
- Schaye J., 2001, *ApJ*, **559**, 507
- Shapiro P. R., Giroux M. L., 1987, *ApJ*, **321**, L107
- Sharma M., Theuns T., Frenk C., Bower R. G., Crain R. A., Schaller M., Schaye J., 2017, *MNRAS*, **468**, 2176
- Shukla H., Mellema G., Iliev I. T., Shapiro P. R., 2016, *MNRAS*, **458**, 135
- Sobacchi E., Mesinger A., 2014, *MNRAS*, **440**, 1662
- Teyssier R., 2002, *A&A*, **385**, 337
- Totani T., et al., 2014, *PASJ*, **66**, 63
- Watkinson C. A., Mesinger A., Pritchard J. R., Sobacchi E., 2015, *MNRAS*, **449**, 3202
- Worseck G., et al., 2014, *MNRAS*, **445**, 1745
- Wyithe J. S. B., Bolton J. S., 2011, *MNRAS*, **412**, 1926

APPENDIX A: PARAMETER VALUES

In Table A1, we give the best-fit values of the parameters in Equation (1) for our simulations, averaged over the five simulations presented in this paper.

APPENDIX B: ROBUSTNESS OF SELECTION OF SELF-SHIELDED SYSTEMS

In order to test the robustness of our Gaussian filtering technique to isolate self-shielded regions, we test here another method to perform this filtering. This technique aims at isolating cells that are in ionization equilibrium. We do this by keeping only cells with $\log_{10}(R) < 0.01$, with R the ratio that gives the number of ionized atoms per second over the number of recombined atoms per second. R is defined as follows:

$$R = \frac{\Gamma x_{\text{HI}}}{\alpha_A n_{\text{H}} (1 - x_{\text{HI}})^2} \quad (\text{B1})$$

Then, we exclude cells that are not yet ionized (i.e. still in neutral region with a photoionization rate $\Gamma = 0$) by keeping only cells with $\Gamma \geq 10^{-17}$. For cells respecting these two criteria, we compute the distribution of Γ as a function of n_{H} . Figure B1 compares this distribution with the one obtained with the Gaussian filtering method used all over the paper. We clearly see that the fits of the distribution with Equation (1) obtained with the two methods are almost indistinguishable, suggesting that the method used all over the paper is robust.

This paper has been typeset from a $\text{\TeX}/\text{\LaTeX}$ file prepared by the author.

Table A1. Best-fit values of the parameters in Equation 1 for our simulations, averaged over the five simulations presented in this paper. They describe the average of the curves in Figure 7. Also shown is the average photoionization rate in ionized regions. Densities are in physical units.

z	Γ_{HI} (10^{-12} s^{-1})	n_0 (cm^{-3})	α_1	α_2	β	f
3.0	1.13	0.0090	-1.12	-1.65	5.32	0.018
4.0	1.05	0.0093	-0.95	-1.50	5.87	0.015
5.0	0.90	0.0103	-1.29	-1.60	5.06	0.024
6.0	0.34	0.0070	-0.94	-1.51	6.11	0.029
7.0	0.07	0.0027	-0.86	-1.27	7.08	0.041
8.0	0.10	0.0040	-0.74	-1.40	7.12	0.041
9.0	0.14	0.0046	-0.64	-1.21	9.99	0.029
10.0	0.20	0.0047	-0.39	-0.86	12.94	0.006

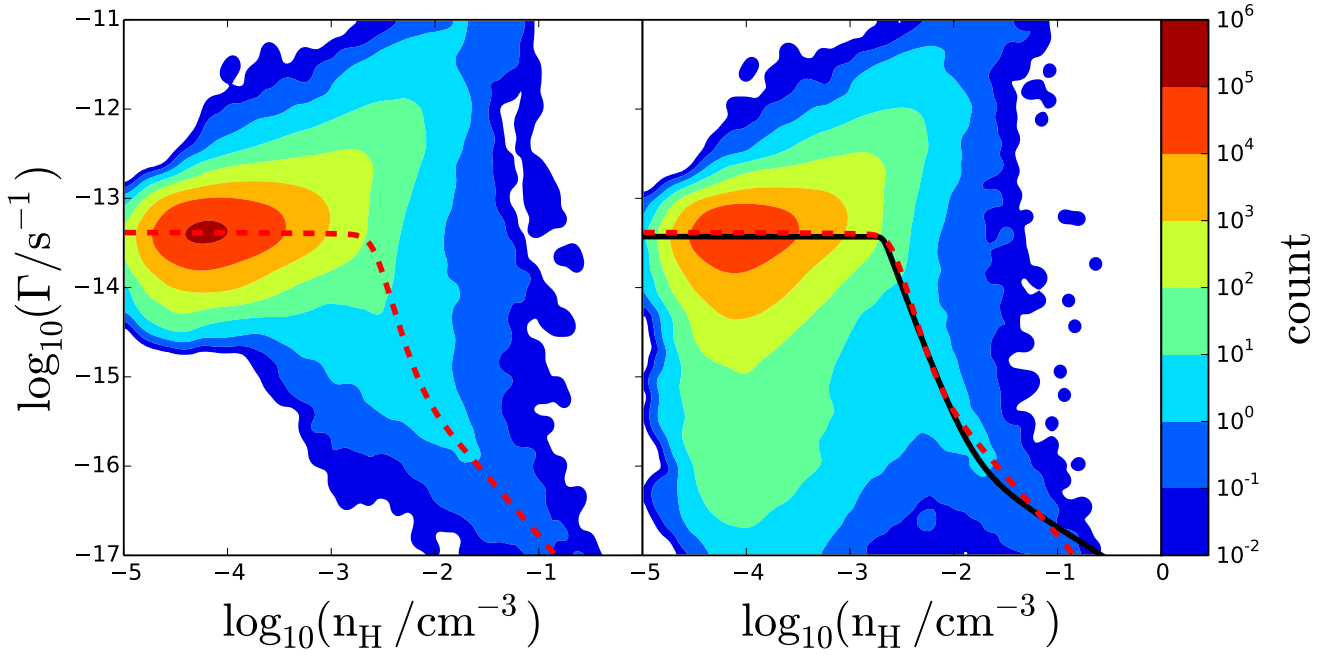


Figure B1. Comparison of two different methods of identifying ionized regions in our radiative transfer simulations. This is same simulation as in Figure 5. Left panel shows the photoionization rate distribution in ionized regions identified using the method presented in the main text. The red dashed curve shows a fit using Equation (1); this curve is reproduced in the right panel for comparison. The left panel is identical to the $z = 7$ panel of Figure 5. The right panel shows the photoionization rate distribution in ionized regions identified using our new selection method. In this method, ionized regions are defined as regions with non-zero photoionization rate that are in ionization equilibrium. Black curve in this panel shows a fit using our Equation (1). The red and black curves in the right panel are virtually identical, which validates the selection method used in this paper.